ORIGINAL PAPER

CrossMark

Effect of SHI on properties of template synthesized Cu nanowires

Rashi Gupta[1] · R. P. Chauhan[2] · S. K. Chakarvarti[2] · Rajesh Kumar[1]

Abstract

Metallic as well as semiconducting nanostructures have generated wide interest and are achieving growing importance because of their potential applications in various devices, such as batteries, manufacturing of electrical contacts in microelectronics, MEMS, and solar cells. In the present work, template synthesis method coupled with electrodeposition has been used to synthesize copper nanowires of diameter 200 nm into the pores of a polycarbonate track-etched (PCTE) membrane. The synthesized Cu nanowires were irradiated with 150-MeV Ti^{9+} swift heavy ions at Inter University Accelerator Centre (IUAC), New Delhi, India. The pristine and irradiated nanowires were characterized by X-ray diffraction (XRD), Scanning electron microscopy (SEM), Energy dispersive spectroscopy (EDS), and Keithley 2400 series source meter to study their structural, morphological, elemental, and electrical properties, respectively. XRD analysis confirmed the face-centered cubic crystal system for pristine as well as irradiated samples. The lattice strain and crystallite size were evaluated using line broadening analysis methods following modified Scherrer method. Theoretical calculations have been done to obtain Young's modulus of the nanowires and that has further been used to evaluate stress generated in the nanowires. Hall-Petch relation has been used to evaluate the change in strengthening coefficient in the nanowires due to irradiation. SEM analysis confirmed the cylindrical morphology of wires with a uniform diameter throughout the complete length of the wires. A change in electrical conductivity of the nanowires has been observed with increase in the fluence which is attributed to change in the orientation of grain boundaries and formation of defects.

Keywords Electrodeposition · Swift heavy ions · X-ray diffraction · Scanning electron microscopy · Mechanical properties · Electrical properties

Introduction

In last few decades, one-dimensional nanostructures like nanowires, nanorods, nanotubes, and nanowhiskers have drawn attention of the researchers worldwide. A number of synthesis techniques are being used to create low dimensional structures, such as photolithography, nanolithography, electrodeposition, chemical vapor deposition, and microcontact printing [1–6]. However, some of these techniques cannot be employed for large-scale industrial fabrications as they are not economical and also time-consuming. In past few years, alternatively few cost-effective and high-output fabrication techniques have been investigated. Kaps et al. [7] have reported a single step flame method for the growth of free standing ZnO nano/microwires. Sanger et al. [8] have deposited vertically ordered Pd-decorated nanocauliflowers on Ag-coated porous anodic alumina substrate by DC magnetron sputtering. Holken et al. [9] have reported the successful cost-effective synthesis of 3D hollow aero-Si nano/microstructure (tetrapods and spheres) by sacrificial template nanotechnology. Kumar et al. [10] have fabricated symmetric supercapacitor based on α-MnO$_2$ nanorods by reactive DC sputtering as it is a versatile and facile method to achieve high-performance combination and binder free electrodes on a large scale. Amongst them, the template-assisted electrodeposition approach can be used to pattern low dimensional structures and allow large-scale synthesis of metal and semiconductor compounds and heterostructures in which optical and electronic properties can be tailored by just altering the constituents, morphology, and dimension distribution [11–14]. The growth mechanism of nanowires using this technique is a multistep process. The deposition of metal into

✉ Rajesh Kumar
rajeshpositron@gmail.com

[1] University School of Basic and Applied Sciences, Guru Gobind Singh Indraprastha University, New Delhi 110078, India

[2] Department of Physics, National Institute of Technology, Kurukshetra 136119, India

pores of the template is associated with mobility-assisted growth model. The first step involves initial nucleation and growth of nuclei of the material we want to deposition inside the pores. The concentration of ions to be deposited has to be high enough to control the hydrogen evolution. The next step is the continuous growth of nuclei which impinge inside the template. The homogenous growth is achieved if the electroactive species migrate towards the channels of the membrane fast enough to travel to the barrier layer. The last step is to cease the deposition at the point when deposition reaches the ends of the pores. Quite often the templates used had been basically the track-etch membranes having the length to diameter ratio in the range 10–1000 and size varying from 10 nm to several μm [15]. The nanostructures synthesized using templates exhibit small roughness and large aspect ratio. The diameter of the wires can be changed by using prefabricated templates (Whatman, Sterlitech) of different dimensions. The nanostructures can be removed from the polymer template by using a suitable etchant, and this is important for their morphological characterization and to study the properties of an isolated nanowire or nanotubule. However, to develop specific devices and to characterize these wires and tubules, they are kept in the host material. Arrays of nanowires of Ag, Fe, Ni, ZnS, and Ag_2Se have been prepared by using this electrochemical deposition approach [16–20]. The freestanding vertically aligned wires can be synthesized by various techniques including flame transport method, lithography, and template-assisted deposition [21, 22]. The wires obtained by template-assisted electrochemical deposition are uniform throughout the complete length, support multilayer deposition, and flexibility for deposition of low dimensional structures of different shapes. The synthesis is possible at low temperatures (< 100 °C) without any need of vacuum that makes it an economic and energy-efficient method (low temp.). The nanowires deposited electrochemically often grow with certain preferential crystallographic orientations that are influenced by electrochemical deposition potentials [23, 24]. Kotok et al. [25] have shown that the 92 nm and 185 nm diameter Au nanowires possess conductivity near to the bulk conductivity if the nanowires are highly crystalline and smooth. Ag and Au nanowires can be used as an ideal interconnect in nanoscale devices due to their excellent properties, but nowadays, copper is widely used as it is abundantly available and less expensive [26].

Swift heavy ions (SHIs) transfer energy in a specific way in the matter in small portions along their path thereby resulting in developments in the field of science and technology on the nanoscale [27–32]. The modifications at the electronic level of any material occur due to a large amount of energy deposition by SHI beams [33]. The changes may be attributed to various factors, such as crosslinking, creation of defect sites in molecular structure, structural rearrangements, and molecular emission. Irradiation generates crystal defects that disturb the periodicity in the crystalline media that leads to variation in electrical properties and mechanical properties [34]. The modifications induced are influenced by the parameter, such as incident ion species, energy, charge state, beam current, and properties (density, crystalline, amorphous, etc.) of the target medium. The modification also depends on the electronic energy loss and nuclear energy loss that are governed by two phenomenological models, i.e., thermal spike model and Coulomb explosion model [35]. According to Coulomb explosion model, the host material is modified on account of ionization produced by the passing SHI along its path followed by electrostatic repulsion and leading to explosion among the charges produced. These SHIs create almost vertical, cylindrical damage trails of diameter 5–10 nm. SHIs create tracks and transfer a notable amount of energy to the matter, which is then transferred to matter resulting in thermal spike. During this process, shooting up of atomic energies takes place for picoseconds resulting in atomic displacement and mass movement. Researchers have irradiated thin films and nanostructures to understand the ion interaction with matter. SHI when enters a material causes modification in properties of the target material by dense electronic excitation, which may not be possible to achieve by conventional methods. Zhao et al. [36] have reported changes in the microstructure that led to change in the degree of hardening on irradiation with He ion. Wang et al. [37] have explained that electrical resistivity of Cu/V multilayer films increases on He ion irradiation due to an increase of the point defects induced by ion irradiation. Singhal et al. [38] have reported modifications in structural, electrical, and optical properties of $Cu-C_{60}$ nanocomposite thin films. Nath et al. [39] have reported that irradiation with 100-MeV Si^{9+} has led to enhancement of electrochemical properties of the ionic liquid nanocomposite polymer electrolyte. The cylindrical damage tracks formed during the process of slowing down of energetic ion in the target material lead to change in structural properties of the pure metals [40]. The damage caused during ion irradiation comprises of two aspects—Frenkel defects and other based on thermal spike [41, 42]. Structural variation in the nanowires results into change in electrical, optical, and mechanical properties [43–45], whereas decrease in the electronic transport properties is due to obstacles produced during irradiation in the path of moving charge carriers that make the flow less smoother than earlier [46]. The directional flow of charge carriers is seized due to irradiation that amputates the ballistic transport and increases the diffusive transport [47]. Our previous work [48] has reported the effect of gamma radiation on copper microstructures; however, the modifications caused due to SHI and gamma rays are completely different from each other. The SHI interacts with materials in both ways, i.e., elastic as well as inelastic, whereas gamma radiation interacts with the material only the way of inelastic interaction. Also, in the previous work published, the pore diameter of the

nanowires was 1 μm, whereas in this work, the pore diameter in 200 nm. Also, few other groups have used SHIs and gamma radiation to study the change in properties of different material. Srivastava et al. [49] and Singhal et al. [50] have tailored the properties of PEDOT: PSS/non-graphite nanocomposites SHI and gamma rays, respectively. The SHI irradiation leads to change in strain and strengthening coefficient of the nanowires. Many reports are not available in the literature that evaluates Young's modulus and explain the change in strain and strengthening coefficient of the nanowires upon irradiation. Herein, we demonstrate a facile template-assisted electrodeposition technique with the reduction of Cu^{2+} ions to Cu using appropriate reduction potential to synthesize Cu nanowires. The as-synthesized nanowires were irradiated with 150-MeV Ti^{9+} ions at four different fluences, viz., 5×10^{10}, 1×10^{11}, 5×10^{11}, and 1×10^{12}. The effect of electronic stopping power $(dE/dX)_e$ on structural and mechanical properties has been investigated. Hall-Petch relation has been used to evaluate the change in strengthening coefficient in the nanowires due to irradiation. A change in electrical conductivity of the nanowires has been explained using Mayadas and Shatzkes (MS), Fuchs & Sondheimer (FS), and electrochemical potential gradient models.

Experimental

Electrodeposition of Cu nanowires

The nanowires were grown in polycarbonate track-etched (PCTE) membrane. Conventional two-electrode setup was used for the cathodic electrodeposition performed under potentiostatic conditions. The template was mounted on top of a conducting copper tape adhesive from one side using transparent plastic tape. The combination of template and Cu tape was pasted over a Cu metal strip that acted as the cathode (working electrode) and a cylindrical copper rod acted as a counter electrode. The schematic representation of the electrochemical cell used during the synthesis is shown in Fig. 1. PCTE membrane with a thickness of 10 μm, pore density 1×10^8 pores/cm^2 and pore diameter 200 nm, purchased from Whatman, were used as templates for the deposition of Cu nanowires. During the electrodeposition, the electroactive species migrating into the nanochannels have to reach the barrier layer quite fast such that homogenous electrodeposition in the pores can be obtained. Also, the concentration of Cu ions has to be sufficient enough to suppress the production of hydrogen evolution. The electrolyte was prepared by dissolving 1M $CuSO_4 \cdot 6H_2O$ in deionized water (MILLI Q 18-MΩ). The pH was adjusted to 1.7 by using concentrated sulfuric acid. The electrodeposition was carried out at 300 K at a potential of − 0.34 V.

Swift heavy ion irradiation

The SHI irradiation was carried out in high vacuum in materials science chamber using a 15 UD Pelletron accelerator at Inter University Accelerator Centre (IUAC), New Delhi, India. The copper nanowires were irradiated with 150-MeV Ti^{9+} ion beam at different fluences of 5×10^{10}, 1×10^{11}, 5×10^{11}, and 1×10^{12} ions/cm^2 keeping the current constant at 0.5 pnA. The energy of Ti^{9+} ion beam was chosen as 150 MeV such that it could completely cross the length of the nanowire. The projected ion range was calculated using transport of ions in matter (TRIM) software. Stopping and range of ions in matter (SRIM) were used to calculate the electronic and nuclear energy losses that were 1.434×10^3 and 1.586 eV/Å, respectively.

Characterizations

The XRD analysis was performed using a Bruker X-ray powder diffractometer having a Cu anode and an X-ray mirror on the primary side. CuKα radiation of wavelength 1.5406 Å, operated at 40 kV and 40 mA was used during investigation. All diffract graphs were examined from 40° to 95° with a step size of 0.02°. Field emission scanning electron microscopy (EVO18, Carl Zeiss) was employed to characterize the morphology of the nanowires. The chemical composition of the synthesized samples was analyzed by energy dispersive X-ray spectroscopy. I-V characteristic (IVC) measurements were done using a Keithley 2400 source meter. The tungsten tip was used as one electrode in two-electrode setup to make contact between the nanowires embedded in the polycarbonate membrane, while Cu tape acted as another electrode during the I-V measurements. At a time, the tungsten probe covered around 80 parallel nanowires and the measurements were carried out in different regions of the PCTE membrane.

Results and discussions

Morphological and EDAX studies

The Scanning electron microscopy (SEM) images of pristine and irradiated Cu nanowires are shown in Fig. 2. SEM has been employed to study the morphology of Cu nanowires as it is the most convenient method to study the peripheral topography of the material. For the morphological study, the PCTE membrane was dissolved in dichloromethane (CH_2Cl_2). The rinsed and dried samples were coated with a 5 nm thin layer of Au-Pd using a Quorum sputter coater to make sample conducting. The samples were viewed under scanning electron microscope (EVO 18 SEM from Carl Zeiss, Germany) at an accelerating voltage 15 kV. Figure 2a, b, c displays SEM images of pristine Cu nanowires of diameter 200 nm at different magnifications.

Fig. 1 Schematic diagram illustrating electrochemical cell used during the synthesis of Cu nanowires
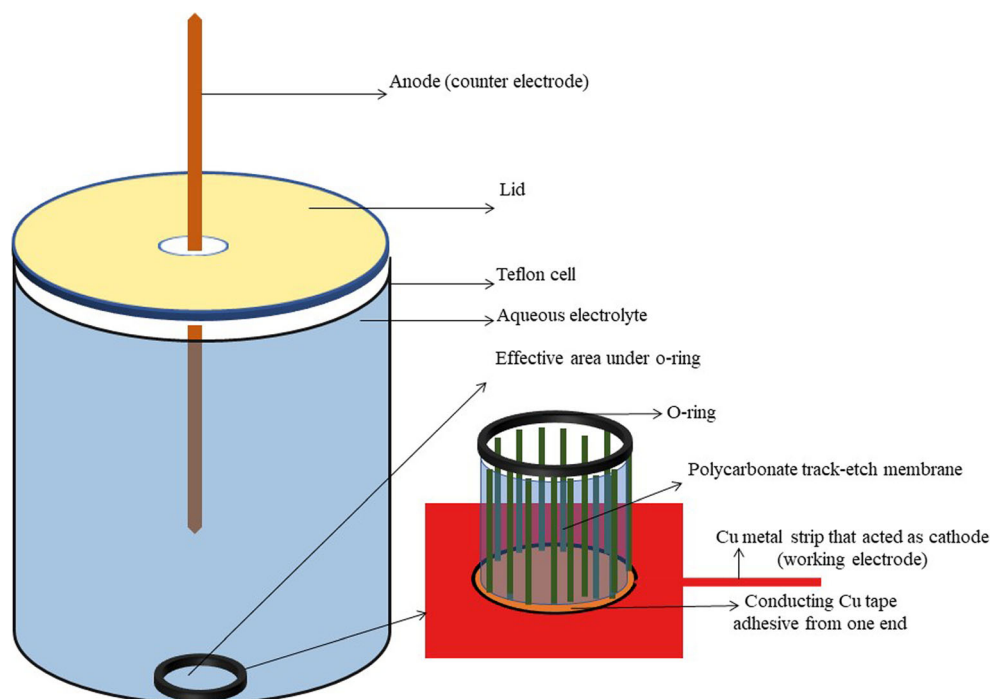

Figure 2d, e manifests SEM images of irradiated nanowires at the minimum (5×10^{10} ions/cm^2) and maximum (1×10^{12} ions/cm^2) fluences, respectively. The SEM studies reveal that the nanowires were standing and have a uniform diameter equal to the diameter of the template in pristine as well as irradiated nanowires. Few wires have aggregated together after the dissolution of the membrane due to the surface tension of the solvent drops. The template-assisted electrodeposited nanowires were found to be highly ordered, smooth, cylindrical shaped, and vertically aligned. The diameter dispersion within

the as-synthesized Cu nanowire sample was only 8%. The average diameter as obtained from Gaussian fit was found to be 205 nm as shown in Fig. 3. No change in the external morphology of the nanowires has been observed after irradiation. The energy dispersive spectroscopy has been used to make the elemental analysis of the as-synthesized Cu nanowires. As the irradiation was performed in vacuum, there were no chances of change in elemental composition during irradiation. The weight% of Cu was found to be 96.65% along with very little oxygen of 3.35% as shown in Fig. 4.

Fig. 2 SEM images of Cu nanowires (**a**, **b**, **c**) pristine at three different magnifications, (**d**) irradiated at fluence 5×10^{10} ions/cm^2, and (**e**) irradiated at fluence 1×10^{12} ions/cm^2
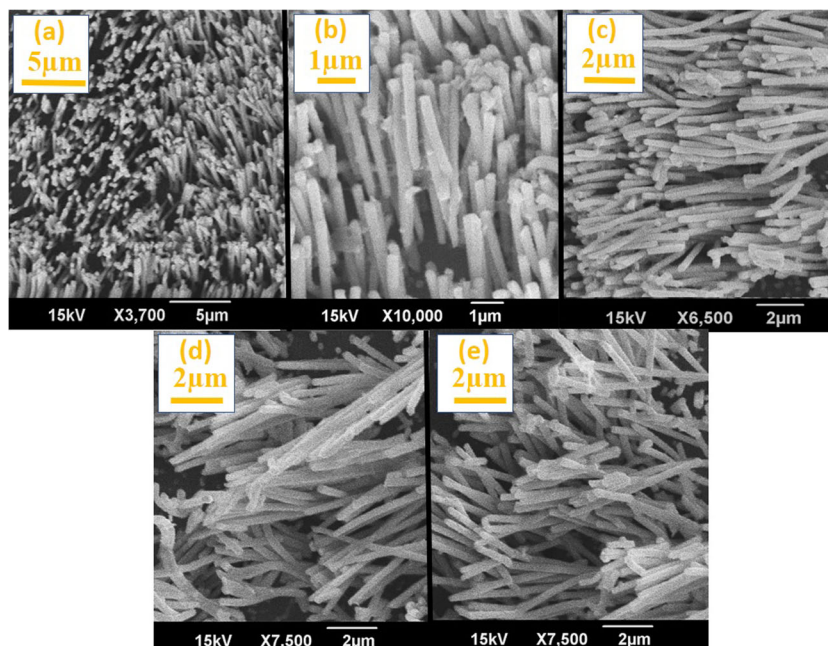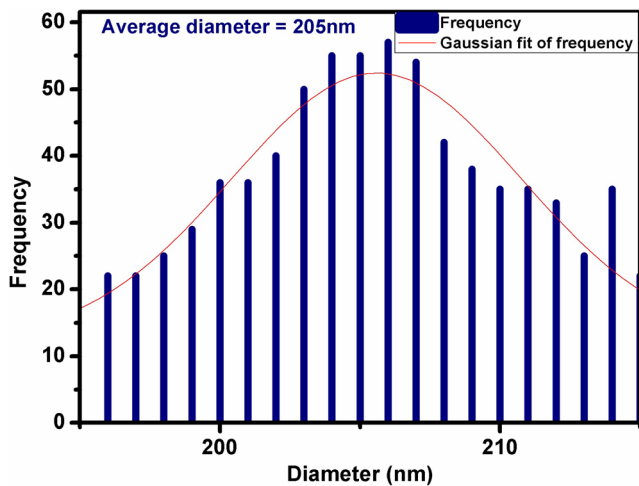
Fig. 3 Histogram showing diameter distribution of pristine Cu nanowire; the Gaussian fit of the data is also displayed

XRD studies

Figure 5 shows the X-ray diffraction (XRD) pattern of pristine and irradiated Cu nanowires. The diffraction peak of the samples, i.e., (111), (200), (220), and (311) at 2θ position (43.31), (50.45), (74.13), and (89.94), respectively, is in good agreement with the standard vaterite polymorph (JCPDS No. 85-1326). The wires could be indexed as a face-centered cubic structure with lattice constant $a =$ 3.165 Å. Crystal planes of different families were present in the XRD pattern that indicated polycrystalline nature of pristine and irradiated nanowires. Variation in relative intensity of peaks was observed with increase in fluence that signifies a change in preferred orientation of the planes in the nanowires upon irradiation. Few other groups have observed similar results [51, 52]. The crystallite size has been evaluated using modified Scherrer method [53, 54].

Peak broadening with crystallite size and lattice strain arising due to dislocation can be calculated using XRD. The width of each XRD peak (δ) is a combined effect of

broadening arising due to sample ($\delta_{measured}$) as well as an instrument ($\delta_{instrument}$). XRD pattern of standard silicon material is used to determine the instrumental broadening. The broadening due to the sample can be evaluated using the relation [55]:

$$\delta = \left[\delta_{measured}^2 - \delta_{instrument}^2\right]. \tag{1}$$

Crystallite size of Cu nanowires was calculated using Debye-Scherrer formula [56–59]:

$$L = \frac{A\lambda}{\delta\cos\theta} \tag{2}$$

where λ is the wavelength of CuK$_\alpha$ radiation (1.54056 Å), A is a constant equal to 0.94, L represents the crystallite size in nanometers, θ is the Bragg peak position, and δ is the peak broadening (radians). On taking the log of Eq. (2),

$$\ln\delta = \ln\frac{A\lambda}{L} + \ln\frac{1}{\cos\theta}. \tag{3}$$

Plotting the values of $\ln\delta$ against $\ln(1/\cos\theta)$, the crystallite size was estimated from the y-intercept of the linear fit curve as shown in Fig. 6. The calculated average crystallite size is given in Table 1. The observed decrease in grain size due to fragmentation results from an inelastic collision between an incident atom and host material. Mallick et al. [60] and Kumar et al. [61] have observed a similar decrease in crystallite size due to SHI irradiation. The change in the grain size results in high density of incoherent interfaces and other defects. The dislocation density (D) and strain (s) were also calculated and shown in Fig. 7. The dislocation density (D) was calculated from Williamson Smallman's formula [62, 63] shown in Eq. (4)

$$D = \frac{n}{L^2} \tag{4}$$

where "n" is a factor taken as unity to obtain minimum dislocation density. The strain (s) [64, 65] developed in the Cu

Fig. 4 Chemical composition of pristine Cu nanowire deposits comprise of 96.65-wt% copper and 3.35-wt% oxygen
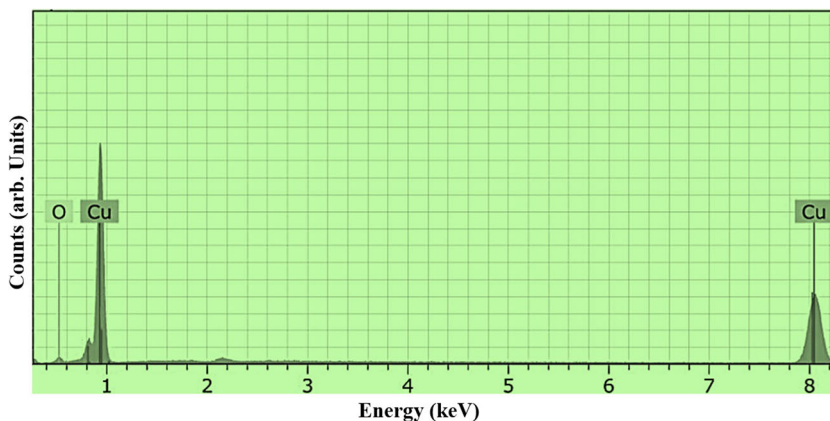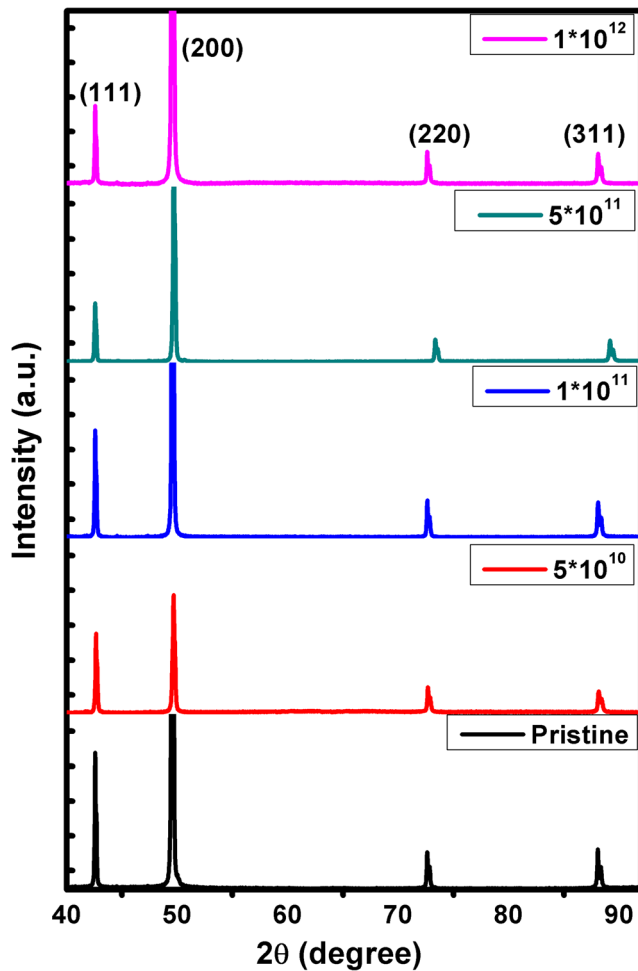
Fig. 5 XRD pattern of pristine and Ti^{9+} ion irradiated nanowires at different fluences of 5×10^{10}, 1×10^{11}, 5×10^{11}, and 1×10^{12} ions/cm^2

nanowires during irradiation was calculated by using the relation shown in Eq. (5)

$$s = \frac{\delta \cot\theta}{4} \tag{5}$$

where "δ" is the full width at half maximum. The strain was obtained from the slope of the linear curve obtained by plotting $4\sin\theta$ vs. $\delta\cos\theta$ as shown in Fig. 8. The strain was generated in the nanowires due to local distortion. As the fluence increases, the energy imparted by the Ti^{+9} ion increases that lead to reorientation of planes. This leads to increase in distortion and strain the nanowires. It has been observed that the dislocation density and the strain are inversely proportional to crystallite size as shown in Table 1.

Mechanical studies

A linear relation between stress and strain generally known as Hooke's law [66, 67]: $Y = \sigma_y/s$, where Y is the Young's
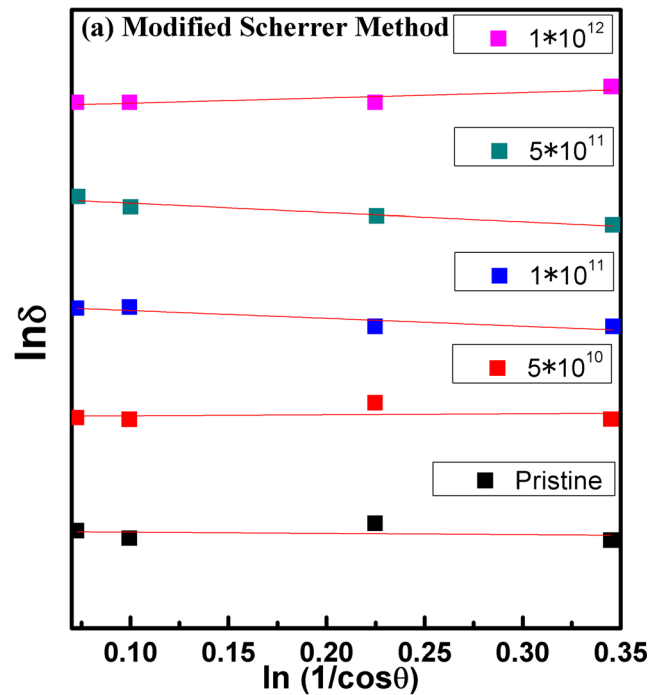

Fig. 6 Modified Scherrer plot of pristine and irradiated Cu nanowires at different fluences of 5×10^{10}, 1×10^{11}, 5×10^{11}, and 1×10^{12} ions/cm^2. Fit the data, the crystallite size L is extracted from the intercept of the fit

modulus of elasticity and σ_y is the stress within the nanowire. The modulus of elasticity (Y_{hkl}) for the cubic crystal system can be theoretically calculated using the relation [68]:

$$Y_{hkl} = [C_{11} - 2[(C_{11} - C_{12}) - 0.5C_{44}]\{l_{12}l_{22} + l_{22}l_{32} + l_{32}l_{12}\}]^{-1} \tag{6}$$

where C_{11}, C_{12}, and C_{44} are the elastic compliances of copper with the values 1.5×10^{-11}, -0.63×10^{-11}, and 1.33×10^{-11} Pa^{-1} respectively. The average Young's modulus for cubic copper nanowires was calculated to be 151.885 GPa. Using the strain values from Table 1 and average Young's modulus, the values of stress obtained are tabulated in Table 1. Increase in stress was observed with increase in ion fluence [69, 70]. As the fluence increases, the time for which the sample remains under irradiation increases that leads the defects to penetrate deeper into the wire layers. But the wires remain under elastic range at all fluences, because we observe an increase in stress with strain. Generation of defects is the cause of atomic stress; as fluence increases, defects increases and that in turn increases the stress in the nanowires. The materials can be strengthened by strengthening their grain boundaries and that can be done by changing the average crystallite size [71]. Herein, we have used SHI irradiation to change the crystallite size and induce stress in the nanowires. Under the generated stress in the nanowires due to irradiation,

Table 1 Crystallite size, Stress, Strain, Dislocation density, Strengthening coefficient, and Resistivity of pristine and irradiated Cu nanowires at different fluences of 5×10^{10}, 1×10^{11}, 5×10^{11}, and 1×10^{12} ions/cm^2

S. no.	Sample name	Crystallite size (nm)	Stress MPa	Strain (10^{-4})	Dislocation density (10^{14} m^{-2})	Strengthening coefficient (k_y) (Pa m$^{-1/2}$)	Resistivity (10^{-6} Ωm)
1	Pristine	51	48.5	3.7	3.84	5303	0.112
2	5×10^{10}	41	121.0	7.9	5.94	19,425	0.117
3	1×10^{11}	47	165.3	10.9	4.52	30,396	0.127
4	5×10^{11}	42	232.0	15.3	5.66	42,400	0.143
5	1×10^{12}	34	263.8	17.4	8.65	44,001	0.197

the dislocations move through the crystal lattice by Frank-Read sources until they encounter grain boundaries. If there is large atomic mismatch within the grain boundaries, dislocations pile up at a grain boundary and are unable to move. These piled up dislocations apply a repulsive force that reduces the energetic barrier for diffusion across the boundary allowing further deformation in the material. As the fluence increases, the grain size decreases; the pile up at the boundary decreases which leads to increase in applied stress required to move the dislocation across the grain boundary. There is an inverse relation between crystallite size and yield strength of the material given by the Hall-Petch equation [72–74]:

$$\sigma_y = \sigma_0 + \frac{k_y}{\sqrt{L}} \quad (7)$$

where σ_y is the stress (given in Table 1), σ_0 is the material constant (for Cu it is equal to 25 MPa [75]), k_y is the strengthening coefficient, and L is the crystallite size. The variation of strain (s) and strengthening coefficient (k_y) with ion fluence are shown in Fig. 9. As the fluence increases, crystallite size decreases; strain also increases that leads to increase in k_y as shown in Table 1. Thus, we can conclude that irradiation with Ti^{9+} ions leads to the strengthening of the nanowires.

Electrical studies

The electrical properties were measured by two-probe method. One probe was attached to the Cu tape and another probe that comprised of tungsten tip of 10-μm diameter was placed exactly on top of the nanowires. The tungsten probe covered some 80 nanowires arranged parallel to each other. A Keithley 2400 source meter was used to measure the equivalent resistance of parallel nanowires by recording the current corresponding to the applied potential, nanowires arranged parallel to each other, and electrical measurements. Figure 10 shows the IV characteristics of pristine and irradiated nanowires. The current (I) vs. potential (V) curve displays fairly linear behavior at room temperature. All *I-V* curves manifest perfect linear dependence, thus exhibiting the ohmic behavior as shown in metals. At room temperature, the resistance of pristine Cu nanowire was about 40.36 Ω. It increases with increase in ion fluence. The resistance of Cu nanowires was calculated from the formula:

$$R_{RT} = \rho \frac{L_H}{A} \quad (8)$$

Fig. 7 Variation of strain (*s*) and dislocation density (*D*) of pristine and irradiated Cu nanowires with ion fluence
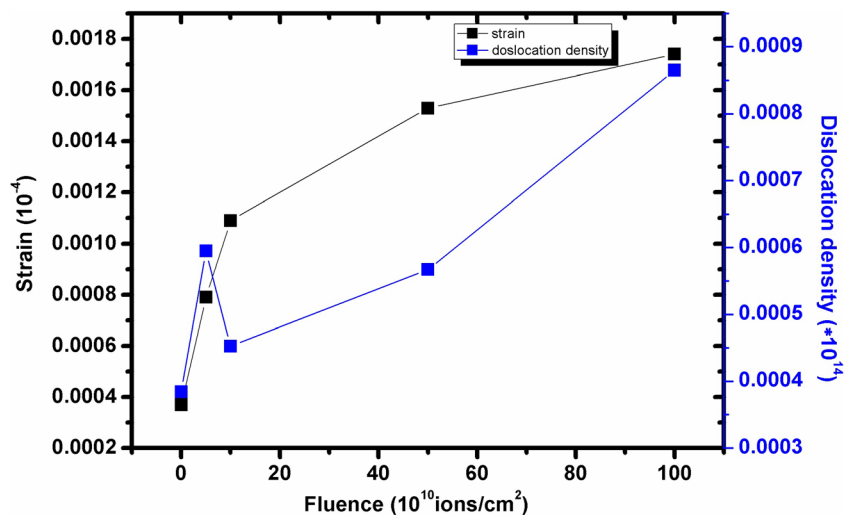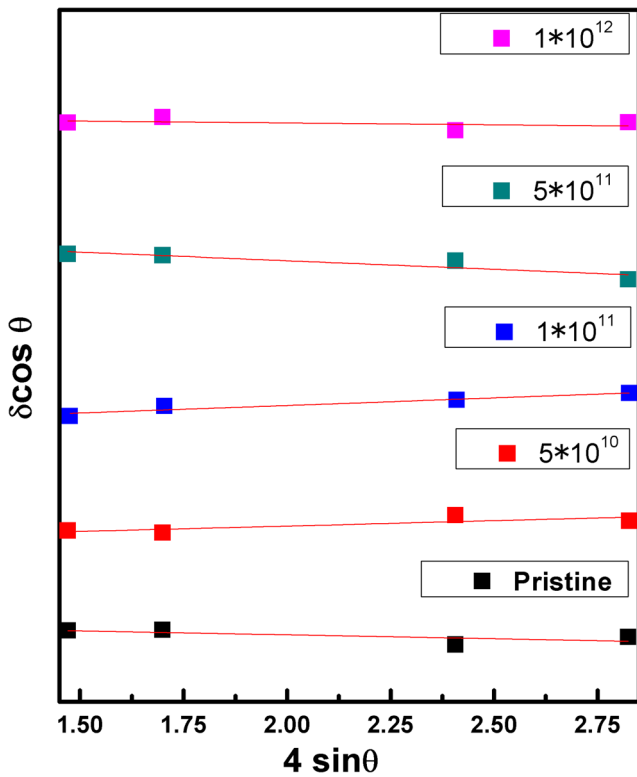
Fig. 8 Strain calculation using the slope of the above liner fit line

where R_{RT} is a resistance at room temperature, ρ is the resistivity, L_H is the length of the nanowire (10 μm), and A is the area of cross section of the Cu nanowire ($A = 3.15$ $(100)^2$ nm^2). The resistivity of pristine nanowire was calculated to be 0.112 μΩm and resistivity increased with increase in ion fluence. The Cu nanowires were polycrystalline in nature, containing many crystal grain boundaries also shown in XRD graph. The average values of grain size obtained from XRD analysis were 51, 41, 47, 42, and 34 nm for pristine and

Fig. 10 *I-V* plot of pristine and irradiated Cu nanowires at different fluences of 5×10^{10}, 1×10^{11}, 5×10^{11}, and 1×10^{12} ions/cm^2. Fit to the data, the resistance R is calculated from the inverse of the slope

irradiated nanowires at fluences 5×10^{10}, 1×10^{11}, 5×10^{11}, and 1×10^{12} ions/cm^2, respectively. A significant decrease in grain size and increase in ion fluence suggest breaking of grains into smaller ones. This would result in increase in grain fragmentation and consequently increase in grain boundary that affects the flow of conducting electrons and increases the resistivity. The collision between incident ions and target atoms creates point defects, and sometimes if target atoms attain enough energy, they even get displaced from its original lattice site. The SHIs deposit their energy in the incident material medium that leads to excitation and ionization in lattice atoms. The primary knock out of atom is followed by the cascade that increases the number of defects. The kinetic energy produced by the Ti^{9+} ion in a cascade is very high that the material is driven outside the thermodynamic equilibrium leading to defect formation. The defects can be like point defects, dislocations, faults, and Frenkel pairs. These defects act as trapping centers for the conduction electrons that leads

Fig. 9 Variation in strain (*s*) and strengthening coefficient (k_y) of pristine and irradiated Cu nanowires with ion fluence

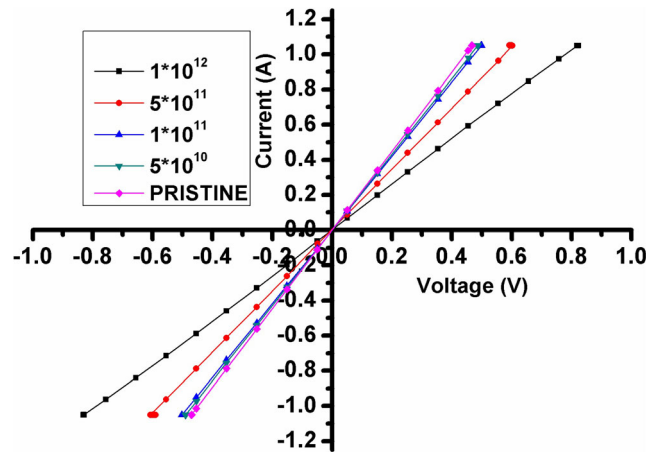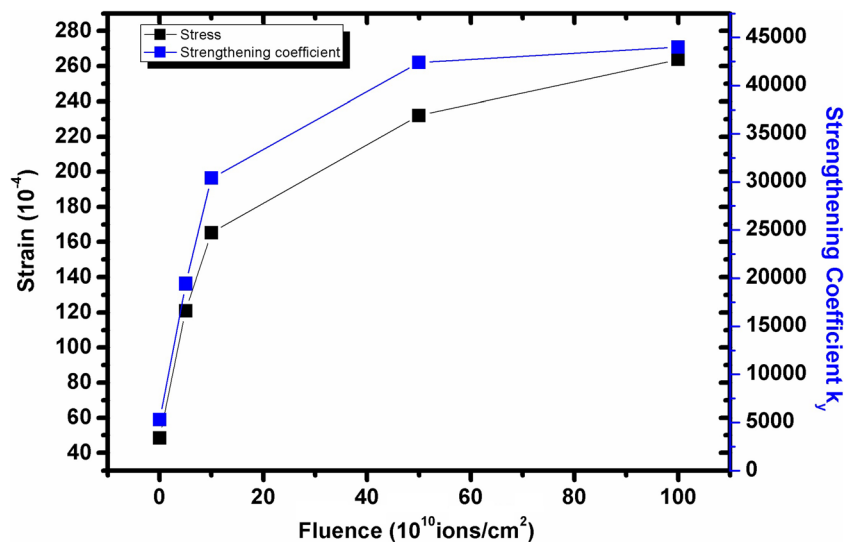to decrease in electrical conductivity. The energy of incident Ti^{9+} ion is 150 MeV; hence, electronic energy loss dominates over nuclear energy loss. The electronic energy loss takes place via ionization and excitation process. This process is also accompanied by recombination of ions and atoms. This recombination and dense electronic excitation and de-excitation process lead to a generation of heat energy, which causes an increase in the amplitude of lattice vibration. The increase in lattice vibration leads to increase in scattering of charge carriers, change in preferred orientation, and diffusion of dislocation and cavities. The scattering of charge carriers from the surface interface and grain boundaries ρ_{M-F} is governed by MS and FS model and can be expressed as [75].

$$\rho_{M-F} = \rho_b \left[1 + \frac{3}{8t}(1-r) + \frac{3}{2}\beta \right] \qquad (9)$$

where ρ_b is the bulk resistivity of Cu equal to 1.68×10^{-8} Ωm, $t = L/\lambda_0$ (L is the crystallite size and λ_0 is the mean free path of electron equal to 40 nm; r is the specularity coefficient equal to 0.5 that describes the fraction of electrons that will be specularly scattered at the wire surface, upon specular scattering, but the dimension of Cu nanowires synthesized for this work has a diameter of 200 nm; so, $\rho_b \frac{3\lambda_0}{8L}(1-r)$ factor will not play a role, $\beta = \lambda_0 R / (1 - R)L$ (R is the grain boundary scattering).

Removing the specularity factor and substituting β in Eq. 9, we get

$$\rho_{M-S} = \rho_b + 0.5 \frac{3\lambda_0}{L} \frac{R}{1-R} \rho_b \qquad (10)$$

ρ_{M-S} is inversely proportional to crystallite size L. Thus, the formation of new grains by fragmentation leads to decrease in crystallite size and increase in resistivity of Cu nanowires with increasing fluence as shown in Fig. 11. Apart from the effectiveness of scattering of charge carriers from defects
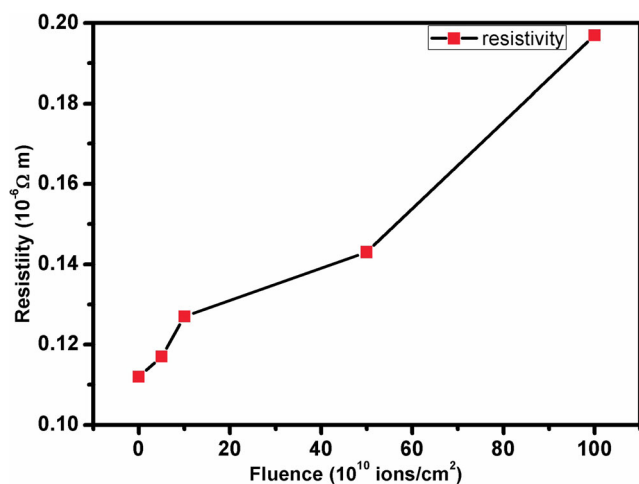

Fig. 11 Variation in resistivity of pristine and irradiated Cu nanowires with ion fluence

and grain boundaries, the electrochemical potential also affects the flow of charge carriers and results into a decrease in electrical conductivity in polycrystalline materials. The flow of charge carriers is influenced by diffusion of electronic and atomic defects. The transport of electric charge is governed by electric potential gradient, and diffusion of atomic defects is governed by the chemical potential gradient. The diffusion mechanism is governed by various parameters like grain boundaries, temperature, porosity, and structure. The net chemical potential would be algebraic sum of potential gradient due to all type of defects. The electrochemical potential gradient for one-dimensional case that governs the flow of charge carriers under the combined effect of chemical and electric potential is given as [76].

$$\frac{d\eta}{dx} = \frac{d\mu}{dx} + z_i e \frac{d\phi}{dx} \qquad (11)$$

where η is the electrochemical potential, μ is the chemical potential, ϕ is the electric potential, and $z_i e$ is the charge of the ith mobile particle. The solution of differential Eq. 11 is

$$\eta = \mu + z_i e\phi \qquad (12)$$

Equation 12 relates the linear combination of chemical and electric potential. The applied electric potential is same for all cases (-1 to 1 V), but chemical potential would be different for each case due to irradiation at different ion fluences. Equation 12 suggests that with the increase in ion fluence, diffusion rate of defects increases which leads to increase in the effective value of chemical potential [76]. At low fluence, the diffusion coefficient would be low and therefore will not play a major role in electrical conductivity, but at higher fluence, the role of chemical potential also becomes important in the net flow of charge carriers that further reduces the electrical conductivity of the nanowires.

Thus, increase in defects and grain boundaries in Cu nanowires combined with an increase in diffusion rate of defects with increasing fluence leads to decrease in electrical conductivity of the nanowires.

Conclusions

Template synthesis method coupled with electrodeposition has been used to synthesize copper nanowires of diameter 200 nm into the pores of a PCTE membrane. The synthesized Cu nanowires were irradiated with 150-MeV Ti^{9+} SHIs at Inter University Accelerator Centre (IUAC), New Delhi, India. SEM analysis confirmed the cylindrical morphology of wires with a uniform diameter throughout the complete length, and no change in external morphology has been

observed in the irradiated nanowires. XRD analysis confirmed the face-centered cubic crystal system for pristine as well as irradiated samples. The crystallite size was calculated using the modified Scherrer equation and found to decrease due to fragmentation of grain boundaries by energy imparted by Ti^{9+} ions. Theoretical calculations have been done to obtain Young's modulus of the nanowires and that has further been used to evaluate stress generated in the nanowires. Hall-Petch relation has been used to evaluate the change in strengthening coefficient in the nanowires due to irradiation. An increase in strengthening coefficient is observed with increase in ion fluence. A change in electrical conductivity of the nanowires has been observed with increase in the fluence, which is attributed to increase in grain boundaries and formation of defects.

Compliance with ethical standards

Conflict of interest The authors declare that they have no conflict of interest.

References

1. Wang X, Yu C, Wu J, Zhang Y (2013) Template-free hydrothermal synthesis of ZnO microrods for gas sensor application. Ionics 19: 355–360. https://doi.org/10.1007/s11581-012-0714-z

2. Wumair T, Dou J, Zhang L, Chen M, Kang X (2013) Synthesis of carbon microtubules core structure LiFePO$_4$ via a template-assisted method. Ionics 19:1855–1860. https://doi.org/10.1007/s11581-013-0916-z

3. Del Valle MA, Hernández LA, Ramírez AM et al (2017) Electrosynthesis of polyquinone nanowires with dispersed platinum nanoparticles toward formic acid oxidation. Ionics 23:191–199. https://doi.org/10.1007/s11581-016-1796-9

4. Singh H, Laibinis PE, Hatton TA (2005) Synthesis of flexible magnetic nanowires of permanently linked core-shell magnetic beads tethered to a glass surface patterned by microcontact printing. Nano Lett 5:2149–2154. https://doi.org/10.1021/nl051537j

5. Choi WK, Liew TH, Dawood MK, Smith HI, Thompson CV, Hong MH (2008) Synthesis of silicon nanowires and nanofin arrays using interference lithography and catalytic etching. Nano Lett 8:3799–3802. https://doi.org/10.1021/nl802129f

6. Stelzner T, Andrä G, Wendler E, Wesch W, Scholz R, Gösele U, Christiansen S (2006) Growth of silicon nanowires by chemical vapour deposition on gold implanted silicon substrates. Nanotechnology 17:2895–2898. https://doi.org/10.1088/0957-4484/17/12/012

7. Kaps S, Bhowmick S, Gröttrup J, Hrkac V, Stauffer D, Guo H, Warren OL, Adam J, Kienle L, Minor AM, Adelung R, Mishra YK (2017) Piezoresistive response of quasi-one-dimensional ZnO nanowires using an in situ electromechanical device. ACS Omega 2:2985–2993. https://doi.org/10.1021/acsomega.7b00041

8. Sanger A, Jain PK, Mishra YK, Chandra R (2017) Palladium decorated silicon carbide nanocauliflowers for hydrogen gas sensing application. Sensors Actuators B Chem 242:694–699. https://doi.org/10.1016/j.snb.2016.11.107

9. Hölken I, Neubüser G, Postica V, Bumke L, Lupan O, Baum M, Mishra YK, Kienle L, Adelung R (2016) Sacrificial template synthesis and properties of 3D hollow-silicon nano- and microstructures. ACS Appl Mater Interfaces 8:20491–20498. https://doi.org/10.1021/acsami.6b06387

10. Kumar A, Sanger A, Kumar A, Mishra YK, Chandra R (2016) Performance of high energy density symmetric supercapacitor based on sputtered MnO$_2$ nanorods. ChemistrySelect 1:3885–3891. https://doi.org/10.1002/slct.201600757

11. Kumar S, Vohra A, Chakarvarti SK (2012) Synthesis and morphological studies of ZnCuTe ternary nanowires via template-assisted electrodeposition technique. J Mater Sci Mater Electron 23:1485–1491. https://doi.org/10.1007/s10854-011-0615-3

12. Liang L, Koshizali N, Li G (2008) Nanotube arrays in porous alumina membranes. J Mater Sci Technol 24:550

13. Movsesyan L, Schubert I, Yeranyan L, Trautmann C, Eugenia Toimil-Molares M (2016) Influence of electrodeposition parameters on the structure and morphology of ZnO nanowire arrays and networks synthesized in etched ion-track membranes. Semicond Sci Technol 31:14006. https://doi.org/10.1088/0268-1242/31/1/014006

14. Kemell M, Pore V, Tupala J, Ritala M, Leskelä M (2007) Atomic layer deposition of nanostructured TiO$_2$ photocatalysts via template approach. Chem Mater 19:1816–1820. https://doi.org/10.1021/cm062576e

15. Schönenberger C, van der Zande BMI, Fokkink LGJ, Henny M, Schmid C, Krüger M, Bachtold A, Huber R, Birk H, Staufer U (1997) Template synthesis of nanowires in porous polycarbonate membranes: electrochemistry and morphology. J Phys Chem B 101:5497–5505. https://doi.org/10.1021/jp963938g

16. Valizadeh S, George JM, Leisner P, Hultman L (2002) Electrochemical synthesis of Ag/Co multilayered nanowires in porous polycarbonate membranes. Thin Solid Films 402:262–271. https://doi.org/10.1016/S0040-6090(01)01674-1

17. Song S, Bohuslav G, Capitano A, du J, Taniguchi K, Cai Z, Sun L (2012) Experimental characterization of electrochemical synthesized Fe nanowires for biomedical applications. J Appl Phys 111: 56103. https://doi.org/10.1063/1.3692068

18. Ertan A, Tewari S, Talu O (2008) Electrodeposition of nickel nanowires and nanotubes using various templates. J Exp Nanosci 3:287–295. https://doi.org/10.1080/17458080802570617

19. Monika, Kumar R, Chauhan RP et al (2015) Preparation and field emission study of low-dimensional ZnS arrays and tubules. J Exp Nanosci 10:126–134. https://doi.org/10.1080/17458080.2013.803614

20. Monika, Kumar R et al. (2013) Preparation and characterization of Ag$_2$Se nanowalled tubules by electrochemical method. Chalcogenide Lett 10:99–104

21. Colli A, Fasoli A, Pisana S, Fu Y, Beecher P, Milne WI, Ferrari AC (2008) Nanowire lithography on silicon. Nano Lett 8:1358–1362. https://doi.org/10.1021/nl080033t

22. Luo R, Cho I, Feng Y, Cai L, Rao PM, Zheng X (2013) Morphological control of heterostructured nanowires synthesized by sol-flame method. Nanoscale Res Lett 8:347. https://doi.org/10.1186/1556-276X-8-347

23. Tian M, Wang J, Kurtz J, Mallouk TE, Chan MHW (2003) Electrochemical growth of single-crystal metal nanowires via a two-dimensional nucleation and growth mechanism. Nano Lett 3: 919–923. https://doi.org/10.1021/nl034217d

24. Zhu Y, Dou X, Huang X et al (2006) Thermal properties of Bi nanowire arrays with different orientations and diameters. J Phys Chem B 110:26189–26193. https://doi.org/10.1021/jp0652493

25. Critchley K, Khanal BP, Górzny MŁ, Vigderman L, Evans SD, Zubarev ER, Kotov NA (2010) Near-bulk conductivity of gold

nanowires as nanoscale interconnects and the role of atomically smooth interface. Adv Mater 22:2338–2342. https://doi.org/10.1002/adma.201000236

26. Xu W-H, Wang L, Guo Z, Chen X, Liu J, Huang XJ (2015) Copper nanowires as nanoscale interconnects: their stability, electrical transport, and mechanical properties. ACS Nano 9:241–250. https://doi.org/10.1021/nn506583e

27. Kucheyev SO, Timmers H, Zou J, Williams JS, Jagadish C, Li G (2004) Lattice damage produced in GaN by swift heavy ions. J Appl Phys 95:5360–5365. https://doi.org/10.1063/1.1703826

28. Kucheyev SO Lattice damage produced in GaN by swift heavy ions. J Appl Phys 95:5360. https://doi.org/10.1063/1.1703826

29. Jaiswal MK, Kanjilal D, Kumar R (2013) Structural and optical studies of 100 MeV Au irradiated thin films of tin oxide. Nucl Instrum Methods Phys Res Sect B Beam Interact Mater Atoms 314:170–175. https://doi.org/10.1016/j.nimb.2013.05.053

30. Williams JS, Kucheyev SO, Tan HH et al (2005) Ion irradiation-induced disordering of semiconductors: defect structures and applications. Philos Mag 85:677–687. https://doi.org/10.1080/14786430412331320008

31. Shojaee SA, Qi Y, Wang YQ, Mehner A, Lucca DA (2017) Ion irradiation induced structural modifications and increase in elastic modulus of silica based thin films. Sci Rep 7:40100. https://doi.org/10.1038/srep40100

32. Khara GS, Murphy ST, Duffy DM (2017) Dislocation loop formation by swift heavy ion irradiation of metals. J Phys Condens Matter 29:285303. https://doi.org/10.1088/1361-648X/aa74f8

33. Biswas A, Gupta R, Kumar N, Avasthi DK, Singh JP, Lotha S, Fink D, Paul SN, Bose SK (2001) Recrystallization in polyvinylidene fluoride upon low fluence swift heavy ion impact. Appl Phys Lett 78:4136–4138. https://doi.org/10.1063/1.1376664

34. Avasthi DK (2000) Some interesting aspects of swift heavy ions in materials science. Curr Sci 78:1297–1302

35. Srivastava SK, Avasthi DK, Pippel E (2006) Swift heavy ion induced formation of nanocolumns of C clusters in a Si based polymer. Nanotechnology 17:2518–2522. https://doi.org/10.1088/0957-4484/17/10/013

36. Zhao M, Liu F, Yang Z, Xu Q, Ding F, Li X, Zhou H, Luo GN (2018) Fluence dependence of helium ion irradiation effects on the microstructure and mechanical properties of tungsten. Nucl Instruments Methods Phys Res Sect B Beam Interact with Mater Atoms 414:121–125. https://doi.org/10.1016/j.nimb.2017.09.002

37. Wang PP, Xu C, Fu EG, du JL, Gao Y, Wang XJ, Qiu YH (2018) The study on the electrical resistivity of Cu/V multilayer films subjected to helium (He) ion irradiation. Appl Surf Sci 440:396–402. https://doi.org/10.1016/j.apsusc.2018.01.072

38. Inani H, Singhal R, Sharma P, Vishnoi R, Ojha S, Chand S, Sharma GD (2017) Electronic excitation induced modifications of structural, electrical and optical properties of Cu-C$_{60}$ nanocomposite thin films. Nucl Instruments Methods Phys Res Sect B Beam Interact Mater Atoms 407:73–79. https://doi.org/10.1016/j.nimb.2017.05.066

39. Nath AK, Kumar A (2014) Swift heavy ion irradiation induced enhancement in electrochemical properties of ionic liquid based PVdF-HFP-layered silicate nanocomposite electrolyte membranes. J Memb Sci 453:192–201. https://doi.org/10.1016/j.memsci.2013.10.061

40. Ossi PM, Pastorelli R (1997) Structural changes induced by fast heavy ion irradiation of pure metals. Nucl Instrum Methods Phys Res Sect B Beam Interact Mater Atoms 122:566–570

41. Brinkman JA (1954) On the nature of radiation damage in metals. J Appl Phys 25:961–970. https://doi.org/10.1063/1.1721810

42. Toulemonde M, Paumier E, Dufour C (1993) Thermal spike model in the electronic stopping power regime. Radiat Eff Defects Solids 126:201–206. https://doi.org/10.1080/10420159308219709

43. Yavuz H, Kaygili O (2011) The effect of gamma-ray irradiation on the electrical conductivity of CuO–PbO glasses. Radiat Eff Defects Solids 166:100–103. https://doi.org/10.1080/10420150.2010.507671

44. Balamurugan B, Mehta BR, Avasthi DK, Singh F, Arora AK, Rajalakshmi M, Raghavan G, Tyagi AK, Shivaprasad SM (2002) Modifying the nanocrystalline characteristics—structure, size, and surface states of copper oxide thin films by high-energy heavy-ion irradiation. J Appl Phys 92:3304–3310. https://doi.org/10.1063/1.1499752

45. Latif A, Khaleeq-ur-Rahman M, Bhatti KA, Rafique MS, Rizvi ZH (2011) Crystallography and surface morphology of ion-irradiated silver. Radiat Eff Defects Solids 166:265–271. https://doi.org/10.1080/10420150.2010.510327

46. Homoth J, Wenderoth M, Druga T, Winking L, Ulbrich RG, Bobisch CA, Weyers B, Bannani A, Zubkov E, Bernhart AM, Kaspers MR, Möller R (2009) Electronic transport on the nano-scale: ballistic transmission and Ohm's law. Nano Lett 9:1588–1592. https://doi.org/10.1021/nl803783g

47. Wharam DA, Thornton TJ, Newbury R, Pepper M, Ahmed H, Frost JEF, Hasko DG, Peacock DC, Ritchie DA, Jones GAC (1988) One-dimensional transport and the quantisation of the ballistic resistance. J Phys C Solid State Phys 21:L209–L214. https://doi.org/10.1088/0022-3719/21/8/002

48. Gupta R, Kumar R, Chauhan RP, Chakarvarti SK (2018) Gamma ray induced modifications in copper microwires synthesized using track-etched membrane. Vacuum 148:239–247. https://doi.org/10.1016/j.vacuum.2017.11.031

49. Srivastava NK, Rattan S, Mehra RM (2009) Effect of γ-ray irradiation on morphology and electrical properties of poly (vinyl chloride)/graphite composites. Polym Eng Sci 49:1136–1141. https://doi.org/10.1002/pen.21366

50. Singhal P, Rattan S (2016) Swift heavy ion irradiation as a tool for homogeneous dispersion of nanographite platelets within the polymer matrices: toward tailoring the properties of PEDOT:PSS/nanographite nanocomposites. J Phys Chem B 120:3403–3413. https://doi.org/10.1021/acs.jpcb.5b11240

51. Adibi F, Petrov I, Greene JE, Hultman L, Sundgren JE (1993) Effects of high-flux low-energy (20–100 eV) ion irradiation during deposition on the microstructure and preferred orientation of Ti$_{0.5}$Al$_{0.5}$N alloys grown by ultra-high-vacuum reactive magnetron sputtering. J Appl Phys 73:8580–8589. https://doi.org/10.1063/1.353388

52. Rani S, Puri NK, Roy SC, Bhatnagar MC, Kanjilal D (2008) Effect of swift heavy ion irradiation on structure, optical, and gas sensing properties of SnO$_2$ thin films. Nucl Instruments Methods Phys Res Sect B Beam Interact Mater Atoms 266:1987–1992. https://doi.org/10.1016/j.nimb.2008.02.062

53. Yadav H, Sinha N, Goel S, Kumar B (2016) Eu-doped ZnO nanoparticles for dielectric, ferroelectric and piezoelectric applications. J Alloys Compd 689:333–341. https://doi.org/10.1016/j.jallcom.2016.07.329

54. Goel S, Sinha N, Yadav H, Godara S, Joseph AJ, Kumar B (2017) Ferroelectric Gd-doped ZnO nanostructures: enhanced dielectric, ferroelectric and piezoelectric properties. Mater Chem Phys 202:56–64. https://doi.org/10.1016/j.matchemphys.2017.08.067

55. Prabhu YT, Rao KV, Kumar VSS, Kumari BS (2014) X-ray analysis by Williamson-Hall and size-strain plot methods of ZnO nanoparticles with fuel variation. World J Nano. Sci Eng 4:21–28. https://doi.org/10.4236/wjnse.2014.41004

56. Kumar R, Singh P, Gupta SK, Gupta R, Jaiswal MK, Prasad M, Roychowdhury A, Chauhan RP, Das D (2017) Radiation induced nano-scale free volume modifications in amorphous polymeric material: a study using positron annihilation lifetime spectroscopy. J Radioanal Nucl Chem 314:1659–1666. https://doi.org/10.1007/s10967-017-5510-9

57. Dhillon RK, Singh P, Gupta SK, Singh S, Kumar R (2013) Study of high energy (MeV) N^{6+} ion and gamma radiation induced modifications in low density polyethylene (LDPE) polymer. Nucl Instruments Methods Phys Res Sect B Beam Interact Mater Atoms 301:12–16. https://doi.org/10.1016/j.nimb.2013.02.014

58. Gupta SK, Gupta R, Singh P, Kumar V, Jaiswal MK, Chakarvarti SK, Kumar R (2017) Modifications in physico-chemical properties of 100 MeV oxygen ions irradiated polyimide Kapton-H polymer. Nucl Instruments Methods Phys Res Sect B Beam Interact Mater Atoms 406:188–192. https://doi.org/10.1016/j.nimb.2017.02.011

59. Singh P, Asad S, Kumar R (2014) Modifications of structural, optical and chemical properties of Li^{3+} irradiated polyurethane and polyetheretherketone. Radiat Phys Chem 96:181–185. https://doi.org/10.1016/j.radphyschem.2013.09.014

60. Kumar V, Kumar R, Lochab SP, Singh N (2007) Effect of swift heavy ion irradiation on nanocrystalline CaS: Bi phosphors: structural, optical and luminescence studies. Nucl Instruments Methods Phys Res Sect B Beam Interact Mater Atoms 262:194–200. https://doi.org/10.1016/j.nimb.2007.06.006

61. Mallick P, Rath C, Prakash J, Mishra DK, Choudhary RJ, Phase DM, Tripathi A, Avasthi DK, Kanjilal D, Mishra NC (2010) Swift heavy ion irradiation induced modification of the microstructure of NiO thin films. Nucl Instruments Methods Phys Res Sect B Beam Interact Mater Atoms 268:1613–1617. https://doi.org/10.1016/j.nimb.2010.02.005

62. Borah MN, Chaliha S, Sarmah PC et al (2008) Effect of substrate temperature on structural properties of thermally evaporated CdSe thin films of different thickness. Optoelectron Adv Mat 2:342

63. Girija K, Thirumalairajan S, Mohan SM (2009) Structural, morphological and optical studies of CdSe thin films from ammonia bath. Chalcogenide Lett 6:351–357

64. Zhao Y, Zhang J (2008) Microstrain and grain-size analysis from diffraction peak width and graphical derivation of high-pressure thermomechanics. J Appl Crystallogr 41:1095–1108. https://doi.org/10.1107/S0021889808031762

65. Bushroa AR, Rahbari RG, Masjuki HH, Muhamad MR (2012) Approximation of crystallite size and microstrain via XRD line broadening analysis in TiSiN thin films. Vacuum 86:1107–1112. https://doi.org/10.1016/j.vacuum.2011.10.011

66. Sahai A, Goswami N (2014) Structural and vibrational properties of ZnO nanoparticles synthesized by the chemical precipitation method. Physical E Low-Dimensional Syst Nanostruct 58:130–137. https://doi.org/10.1016/j.physe.2013.12.009

67. Yousefi R, Zak AK, Jamali-Sheini F (2013) Growth, X-ray peak broadening studies, and optical properties of Mg-doped ZnO nanoparticles. Mater Sci Semicond Process 16:771–777. https://doi.org/10.1016/j.mssp.2012.12.025

68. Chen W-H, Cheng H-C, Yu C-F (2016) The mechanical, thermodynamic, and electronic properties of cubic Au$_4$Al crystal via first-principles calculations. J Alloys Compd 689:857–864. https://doi.org/10.1016/j.jallcom.2016.08.050

69. Lu C, Jin K, Béland LK, Zhang F, Yang T, Qiao L, Zhang Y, Bei H, Christen HM, Stoller RE, Wang L (2016) Direct observation of defect range and evolution in ion-irradiated single crystalline Ni and Ni binary alloys. Sci Rep 6:19994. https://doi.org/10.1038/srep19994

70. Kharisov BI, Kharissova OV, Mendez UO (2013) Radiation synthesis of materials and compounds. CRC Press, Boca Raton.

71. Callister WD (2005) Fundamentals of materials science and engineering, 2nd edn. Wiley, New York, p 252

72. Zhu YZ, Wang SZ, Li BL, Yin ZM, Wan Q, Liu P (2014) Grain growth and microstructure evolution based mechanical property predicted by a modified Hall–Petch equation in hot worked Ni$_{76}$Cr$_{19}$AlTiCo alloy. Mater Des 55:456–462. https://doi.org/10.1016/j.matdes.2013.10.023

73. Furukawa M, Horita Z, Nemoto M, Valiev RZ, Langdon TG (1996) Microhardness measurements and the Hall-Petch relationship in an AlMg alloy with submicrometer grain size. Acta Mater 44:4619–4629. https://doi.org/10.1016/1359-6454(96)00105-X

74. Smith A, William F, Javad H (2006) Foundations of materials science and engineering, 4th edn. McGraw-Hill, Boston

75. Zheng P, Gall D (2017) The anisotropic size effect of the electrical resistivity of metal thin films: tungsten. J Appl Phys 122:135301. https://doi.org/10.1063/1.5004118

76. Kofstad P, Norby T (2007) Defects and transport in crystalline solids. University of Oslo, Oslo